RSC Advances

COMMUNICATION

View Article Online
View Journal | View Issue

Cite this: *RSC Adv.*, 2016, **6**, 57261

Received 5th May 2016
Accepted 8th June 2016

DOI: 10.1039/c6ra11681g

www.rsc.org/advances

Structural evolution induced preferential occupancy of designated cation sites by Eu^{2+} in $M_5(Si_3O_9)_2$ (M = Sr, Ba, Y, Mn) phosphors†

Yi. Wei,‡[a] Chun Che Lin,‡*[c] Zewei Quan,[d] Maxim S. Molokeev,[ef] Victor V. Atuchin,[ghi] Ting-Shan Chan,[j] Yujun Liang,[a] Jun Lin*[b] and Guogang Li*[a]

In this paper, we present new insight into a changing Eu^{2+} crystallographic site preference in Eu-doped $M_5(Si_3O_9)_2$ (M = Sr, Ba, Y, Mn), which is related to the structural variation induced by M cation substitutions. The effect of the local structural geometry on the luminescence properties of Eu^{2+} is revealed. By substitution of Ba^{2+} for Sr^{2+}, the lattice expansion is restricted to specific cation sites, resulting in the abrupt blue shifted emission of Eu^{2+} ions. The abnormal blue shift on replacing Sr^{2+} with Mn^{2+} is attributed to the preferential 6-fold coordination for Mn^{2+} that moves the Eu^{2+} ions to other sites. The results elucidate the mechanisms of emission band adjustment by local site coordination change and it can be potentially extended to crystals which properties are sensitive to local lattice variations.

Rare-earth-activated silicates are widely used as phosphor materials for white light-emitting diode (WLED) illumination because of their high quantum efficiency and low cost.[1–3] However, unsatisfactory thermal stability and spectral position of the excitation/emission bands limit the applications of these materials. To overcome these disadvantages, different cation substitutions were used to adjust the spectroscopic parameters of silicate phosphors, and numerous corresponding mechanisms were proposed to elucidate the relationship of the structural and luminescence properties. These mechanisms include the "cation size mismatch", "neighboring cation substitution", "nanosegregation and neighbor cation control" and "chemical unit co-substitution" effects.[4–12] However, these mechanisms cannot ultimately solve all problems, and many questions remain unanswered. To date, the cation substitution effect, which can systematically tune spectral position and thermal quenching by changing the coordination environment of the selected cation sites and controlling the preferential activator ion occupancies, has rarely been considered. In the present study, we present a new insight into the structural variation induced site-preferential occupancy of Eu^{2+} in $M_5(Si_3O_9)_2$ (M = Sr, Ba, Y, Mn) phosphors through size-mismatched cation substitutions applicable to spectral positions and thermal stability tuning.

In this study, the $Sr_{2.97-x}Ba_xEu_{0.03}Y_2(Si_3O_9)_2$ (Ba series) and $Sr_{2.97-y}Mn_yEu_{0.03}Y_2(Si_3O_9)_2$ (Mn series) solid solutions ($0 \le x \le 1.59$, $0 \le y \le 0.63$) were successfully prepared. The doping concentration of Eu^{2+} was controlled at the level of 1 at% of Sr^{2+} in the $Sr_3Y_2(Si_3O_9)_3$ host. The synthesis route and characterization description can be found in ESI.† Firstly, the phase composition and structural properties of the samples were identified by XRD analysis. For Ba series, all diffraction peaks of the compounds with $x = 0$, 0.06 and 0.09 were indexed in the monoclinic cell ($C2/c$) of $Sr_3Y_2(Si_3O_9)_3$, as plotted in Fig. S1 (ESI†) and Fig. 1a.[13] A similar $C2/c$ cell was obtained for the composition range of $0.18 < x < 1.59$. However, a noticeable difference was observed in the diffraction patterns in comparison with those recorded from the low-doped samples (Fig. S1

[a]*Faculty of Materials Science and Chemistry, China University of Geosciences, Wuhan 430074, P. R. China. E-mail: ggli8312@gmail.com*

[b]*State Key Laboratory of Rare Earth Resource Utilization, Changchun Institute of Applied Chemistry, Chinese Academy of Sciences, Changchun 130022, P. R. China. E-mail: jlin@ciac.ac.cn*

[c]*Condensed Matter and Interfaces, Debye Institute for Nanomaterials Science, Utrecht University, Princetonplein 5, 3584 CC Utrecht, The Netherlands. E-mail: cclin0530@gmail.com*

[d]*Department of Chemistry, South University of Science and Technology of China, Shenzhen, Guangdong 518055, P. R. China*

[e]*Laboratory of Crystal Physics, Kirensky Institute of Physics, Siberian Branch of the Russian Academy of Sciences, Krasnoyarsk 660036, Russia*

[f]*Department of Physics, Far Eastern State Transport University, Khabarovsk 680021, Russia*

[g]*Laboratory of Optical Materials and Structures, Institute of Semiconductor Physics, SB RAS, Novosibirsk 630090, Russia*

[h]*Functional Electronics Laboratory, Tomsk State University, Tomsk 634050, Russia*

[i]*Laboratory of Semiconductor and Dielectric Materials, Novosibirsk State University, 2 Pirogov Str., Novosibirsk 630090, Russia*

[j]*National Synchrotron Radiation Research Center, Hsinchu 300, Taiwan*

† Electronic supplementary information (ESI) available: Experimental details, Rietveld structural refinement processing and parameters, XRD patterns, Raman spectra, PLE and PL spectra, CIE color coordinates, including Fig. S1–S27 and Tables S1–S3, for $Sr_{2.97-x}Ba_xEu_{0.03}Y_2(Si_3O_9)_2$ (x = 0–1.59) and $Sr_{2.97-y}Mn_yEu_{0.03}Y_2(Si_3O_9)_2$ (y = 0–0.63) compounds. See DOI: 10.1039/c6ra11681g

‡ These authors contribution to this work are equal.

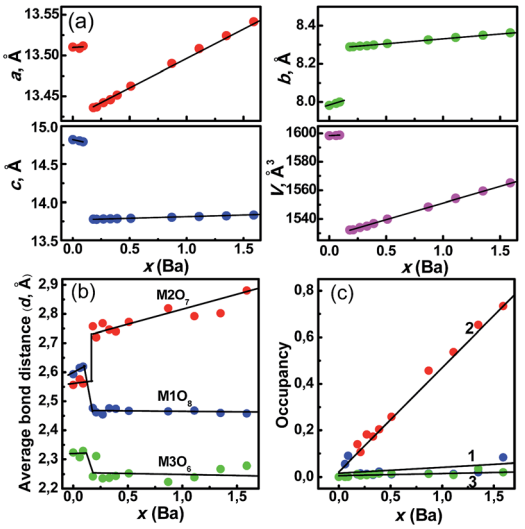

Fig. 1 (a) Dependence of cell parameters *a*, *b*, *c* and cell volume *V* on concentration *x* (Ba) in $Sr_{3-x}Ba_xY_2(Si_3O_9)_2$: Eu ($0 < x \leq 1.59$); dependence on concentration *x* (Ba) of: (b) average bond length: *d*(M1–O) ($M1O_8$), *d*(M2–O) ($M2O_7$), *d*(M3–O) ($M3O_6$); (c) occupancies of M1 site (line 1), M2 site (line 2) and M3 site (line 3) by Ba ions.

(ESI†)), implying a possible phase transition induced by the substitution of Ba^{2+} for Sr^{2+}. Accordingly, these phases can be reasonably differentiated as Phase 1 ($0 \leq x \leq 0.09$) and Phase 2 ($0.18 < x \leq 1.59$). Samples with $x = 0.12, 0.15, 0.18$ represent the mixture of these two phases. Notably, the pure phase state of the Ba series is destroyed at $x > 1.59$, and many impurities appeared, including, besides $(Sr,Ba)_3Y_2(Si_3O_9)_2$, the known silicates $BaSi_2O_5$, $Ba_5Si_8O_{21}$ and $BaY_2Si_3O_{10}$ (Fig. S1 (ESI†)). Thus, the structural analysis was mainly focused on the evolution from Phase 1 to Phase 2.

The evident chemical shift from ~604.2 to ~650.4 cm^{-1} at $x \sim 0.15$ was observed for the representative band from the Raman spectra of the Ba series, verifying the phase transition emergence, as shown in Fig. S2 (ESI†). To determine the effect of this phase transition on the coordination environment of M (Sr/Ba/Y/Eu) ions, Rietveld refinement was performed for the Ba series. The crystal structure of $Sr_3Y_2(Si_3O_9)_2$ was taken as a starting point,[13] The refinement parameters and cell parameters *a*, *b*, *c*, and *V* are presented in Table S1, Fig. S3–S17 (ESI†), and Fig. 1a. The chemical composition of the compounds was close to the nominal compositions, as obtained by the inductively coupled plasma element analysis (Table S2, (ESI†)). Thus, the total site occupancies were constrained during refinement in accordance to the designed compositions. As shown in Fig. 1a, the linear increase of cell parameters and volume on the Ba concentration increase at $x < 0.09$ and $x > 0.18$ in accordance with Vegard's rule proves the solid solution formation at Phase 1 and 2 ranges. The cell parameter jump appeared at $x \sim 0.15$. The *a* and *c* values markedly decreased at $x \sim 0.15$, whereas *b* increases abruptly.

Unexpectedly, *V* noticeably decreases at $x \sim 0.15$, as the Ba concentration increase should imply a cell volume increase. This situation is unusual and it may lead to an unexpected change in the coordination environment of Eu^{2+}.

According to the refinement results (Table S1, (ESI†)), three cation sites M1, M2 and M3 (M1 : M2 : M3 = 2 : 2 : 1) in $M_5(Si_3O_9)_2$ are coordinated with eight ($M1O_8$), seven ($M2O_7$) and six ($M3O_6$) oxygen atoms, respectively. The calculated average bond lengths (*d*) for the M1, M2 and M3 sites are shown in Fig. 1b. At $x \leq 0.09$, all bond lengths slightly increase when the smaller Sr^{2+} ions are gradually substituted with larger Ba^{2+} ions. This result is attributed to the random distribution of Ba^{2+} ions over the three sites in Phase 1. Further, at $0.09 < x \leq 0.18$, *d*(M2–O) exhibits a sharp increase from 2.56 Å to 2.75 Å, while *d*(M1–O) (2.62 → 2.48 Å) and *d*(M3–O) (2.32 → 2.24 Å) decrease. Consequently, the polyhedra $M1O_8$ and $M3O_6$ decrease in size, and only $M2O_7$ polyhedron expands during phase transition. In Phase 2, only *d*(M2–O) increases with *x*, whereas both *d*(M1–O) and *d*(M3–O) basically remain constant. This result indicates that Ba^{2+} ions preferentially substitute Sr^{2+} ions at M2 sites. The opposite bond length changes during phase transition are responsible for the cell volume decrease (Fig. 1a). In addition, the dependence of occupancies in the three sites was investigated. It is clearly shown in Fig. 1c (line 2) that only M2 sites were occupied by Ba^{2+} ions after the phase transition, whereas M1 and M3 were preferential sites for Y^{3+} ions. To emphasize the main features of phase transition associated with three M (Sr/Ba/Y/Eu) sites, the model of structural transformation was built, as shown in Fig. 2a and b. $Sr_3Y_2(Si_3O_9)_2$: Eu consists of Sr/Y/Eu atom layers and Si_3O_9 ring layers.[14] The cube, monocapped trigonal prism and octahedron for M–O share two O atoms with each other. Owing to the phase transition, $M1O_8$ changes from the cube to square antiprism because of the several M1–O bond rotations. This finding indicates a more compact Si_3O_9 unit packing around the M1 sites with reducing *d*(M1–O) and the volume (Fig. 1b). The preferential occupation of $M3O_6$ octahedron by smaller Y^{3+} ions results in a shrinkage of this polyhedron.

Monocapped trigonal prism $M2O_7$ is markedly shrank along the *c*-axis direction from 2.67 Å to 2.42 Å (Fig. 1b). All these shrinkages in the M sites finally lead to the cell volume decrease and a shrinkage between two SiO_4 polyhedra. Although the

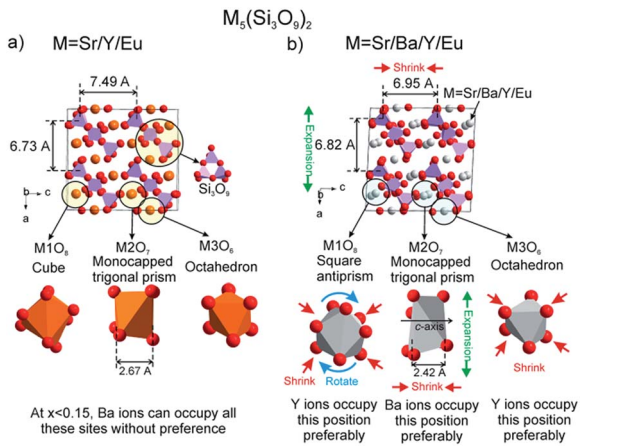

Fig. 2 Mechanism of crystal structure transformation from (a) $Sr_3Y_2(Si_3O_9)_2$: Eu (Phase 1, $x = 0$) to (b) $Sr_{3-x}Ba_xY_2(Si_3O_9)_2$: Eu (Phase 2, $x = 1.59$).

shrinkage occurs along the *c*-axis of the $M2O_7$ polyhedron, the final *d*(M2–O) increases and is, particularly, increasing abruptly during phase transition. This abnormal phenomenon originates from the expansion along the *a*- and *b*-axes. This situation also causes the expansion between two SiO_4 polyhedra along the *a*-axis direction. Generally, with the Ba^{2+} content increase from the phase transition point, only $M2O_7$ polyhedra expand, whereas $M1O_8$ and $M3O_8$ polyhedra shrink regardless of a final increase in the cell volume. Therefore, Ba^{2+} ions preferably occupy the M2 site, whereas the M1 and M3 sites are preferential for Y^{3+} ions.

The 5d–4f transition of Eu^{2+} is sensitive to the structural variation of the host lattice that even a slight change in the local coordination environment around Eu^{2+} can cause a big effect for its luminescence.[15–20] The photoluminescence excitation (PLE) and emission (PL) spectra of the Ba series are shown in Fig. 3a and b, respectively. For $x = 0$, the PLE consists of a broad band from 250 to 430 nm with the maximum at 365 nm. Under 365 nm UV, a bluish-green emission is given with CIE color coordinates (0.168, 0.258). The PL spectrum covers a broad range from 425 to 575 nm, centered at 474 nm. The asymmetric emission results from the three Sr^{2+} sites available for Eu^{2+}, as shown by the three Gaussian fitting peaks at 21 978 cm^{-1} (455 nm), 20 833 cm^{-1} (480 nm), and 19 231 cm^{-1} (520 nm) at M1, M2 and M3 sites (Fig. 3b). With the Ba^{2+}-doping in Phase 1, a slight blue shift emission from 474 nm ($x = 0$) to 469 nm ($x = 0.09$) was observed, as shown in Table S3 and Fig. S18 (ESI†). This shift is attributed to random occupation of larger Ba^{2+} over Sr^{2+} sites in Phase 1 and the resulting cell enlargement. Thus, the crystal field splitting (CFS) of Eu^{2+} 5d energy levels in these enlarged sites weakened, resulting in blue shift emission. During the phase transition, the large blue shift emission from 468 to 438 nm occurred. The result implied that the lattice environment around Eu^{2+} became looser, and thus the average Eu–O bond length (*d*) increased. Generally, the crystal field strength is proportional to $1/d^5$ Therefore, Eu^{2+} ions in the looser sites with the longer bond length will possess a higher energy emission and it will generate a blue shift of the emission band.

In view of the size-difference between Ba^{2+} ions and Sr^{2+} ions, the coordination environment of M ions would change with the Ba^{2+} doping, which could be depicted by the change of *d*(M–O). The *d*(M–O) values at different Ba-doping concentration can be calculated on the base of XRD measurements of the studied samples. According to the refinement results, *d*(M2–O) increases from 2.56 Å to 2.75 Å on the Ba content increase in the transition phase, whereas *d*(M1–O) and *d*(M3–O) slightly decrease. Therefore, Eu^{2+} ions should occupy the looser M2 sites and generate a large decrease in CFS of 5d energy levels of Eu^{2+}, leading to the abnormal large-scale blue shift. This evident blue shift emission during phase transition can be more clearly observed from the color coordinates: (0.161, 0.205) for $x = 0.09$ and (0.157, 0.073) for $x = 0.21$. Given $0.18 < x \leq 1.59$, the crystal structure of the Ba series stabilizes at Phase 2, and the small blue shift from 438 nm at $x = 0.18$ to 432 nm at $x = 1.59$ mainly originates from a continuous decrease in CFS of the 5d energy levels of Eu^{2+} in view of the gradual increase of *d*(M2–O) with *x*. Given $x > 1.59$, the stable structure was destroyed, and numerous foreign phases appeared. Hence, certain low-energy emission peaks emerged, generating a broadened emission and red shift, as shown in Fig. S19 (ESI†). Generally, a large spectral blue shift in the Ba series was induced by the change in the crystal field environment at specific cation sites because of the phase transition. Thus, it offers a novel and efficient route to tune the optical properties of phosphor materials.

On the basis of the same principle, a spectral red shift can be expected in the Mn series because of the enlarged CFS of Eu^{2+} by the substitution of smaller Mn^{2+} for larger Sr^{2+}. Actually, unusual blue shifts in the Mn series spectra were observed with the Mn^{2+} content (*y*) increase, as shown in Fig. 4a and b. To reveal the mechanism of the luminescence blue shift, the phase purity and structure variation in the Mn series were first analyzed by XRD and Rietveld refinement. Evidently, the Mn series samples crystallize in the monoclinic $Sr_3Y_2(Si_3O_9)_2$ phase, space group *C*2/*c*, and the XRD diffraction peaks continuously shift to larger angles with the *y* increase, as shown in Fig. S20 (ESI†). This is in agreement with Vegard rule, revealing the solid solution formation.[4] For the Mn series, the refinement results are presented in Table S4 and Fig. S21–S26 (ESI†). The results verify the generation of host-type structures due to Mn/Eu doping. The cell volume decrease with the *y* increase reflects the formation of Mn series solid solutions (Fig. S27 (ESI†)).

As shown in Fig. 4a, at $y < 0.45$, the PLE spectra of the Mn series are similar to those of the Ba series, except for the maximum at 355 nm. The PL spectra consist of two broad bands in the range of 400–650 nm, which are centered at 472 nm and 545 nm, respectively. The first band is attributed to the 5d–4f transition of Eu^{2+}, whereas the second band is related to the $^4T_{1g}(^4G)$–$^6A_{1g}(^6S)$ transition of Mn^{2+}. Notably, the emission positions of the Eu^{2+} and Mn^{2+} bands remain persistent up to Mn^{2+} doping content $y \sim 0.45$. However, the emission intensity of the Mn^{2+} band gradually increased with the *y* increase, whereas the Eu^{2+} emission intensity first increases and then decreases. Thus, a tunable single-composition white light

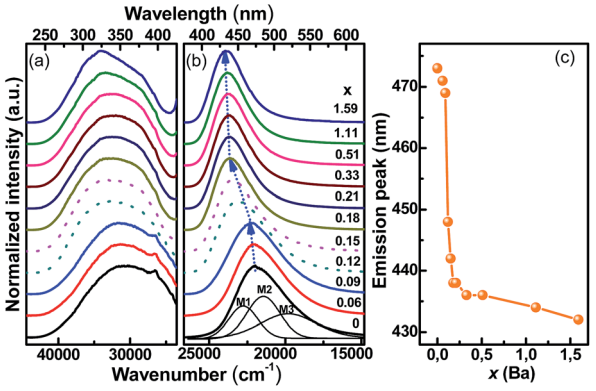

Fig. 3 (a) The photoluminescence excitation (PLE) and (b) photoluminescence emission (PL) spectra of $Sr_{2.97-x}Ba_xEu_{0.03}Y_2(Si_3O_9)_2$ ($x = 0$–1.59) recorded at maximal emission and excitation wavelengths, respectively. The emission peak of $Sr_{2.97}Eu_{0.03}Y_2(Si_3O_9)_2$ was decomposed by Gaussian fitting. (c) The dependence of the emission peaks of Ba series on concentration *x* (Ba).

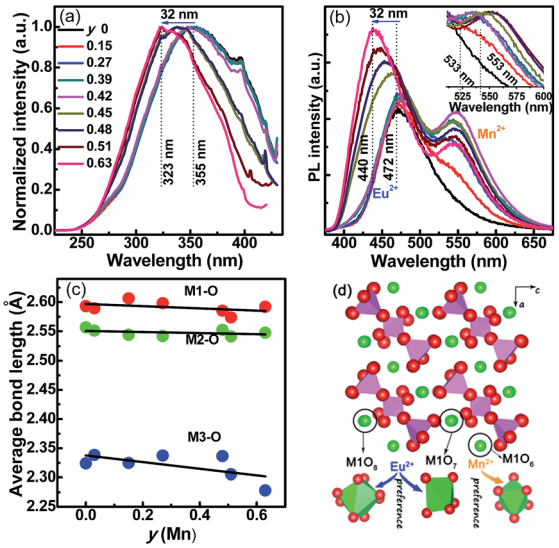

Fig. 4 (a) PLE and (b) PL spectra of $Sr_{2.97-y}Mn_yEu_{0.03}Y_2(Si_3O_9)_2$ ($y = 0$–0.63, Mn series) samples. The normalized PL spectra ranging from 510 nm to 600 nm of Mn^{2+} emission are shown in the insert. (c) Average bond length (Å) [d(M1–O), d(M2–O) and d(M3–O)] as a function of doping concentration y (Mn). (d) A schematic explanation of the preferential occupancy of Eu^{2+} and Mn^{2+} ions in Mn series.

emission can be obtained by mixing blue-green light (Eu^{2+}) and yellow light (Mn^{2+}). Beyond $y = 0.45$, sudden and converse emission shifts for Eu^{2+} (blue shift) and Mn^{2+} (red shift) were observed, as shown in Fig. 4b. The red shift of Mn^{2+} emission is reasonable, as the cell volume of Mn series shrinks with the y increase because of the smaller Mn^{2+} size in comparison with Sr^{2+}, thus enlarging the CFS of the Mn^{2+} 5d levels. However, evident blue shifts of Eu^{2+} emission appeared in the PLE and PL spectra, shifting to 32 nm (355 → 323 nm) and 32 nm (472 → 440 nm), respectively. The results indicate that Mn^{2+} and Eu^{2+} ions exhibit preferential lattice site occupancies in the Mn series solutions. The average M–O bond lengths as a function of y in the Mn series are arranged in Fig. 4c. With changing y from 0 to 0.63, only d(M3–O) exhibits the shrinkage, whereas both d(M1–O) (a slight decrease) and d(M2–O) are almost constant. This implies that Mn^{2+} ions are more easily coordinated with six oxygen atoms, following the priority of $MnO_6 > MnO_8 > MnO_7$. Therefore, a possible mechanism is proposed for the abnormal blue shift of Eu^{2+} emission (Fig. 4d). At low Mn^{2+} doping levels ($y < 0.45$), Eu^{2+} and Mn^{2+} ions randomly enter M1–M3 sites. At $y > 0.45$, the d(M3–O) is lower than 2.33 Å, which is smaller than the sum of Eu^{2+} and O^{2-} ion radii [$r(Eu^{2+}) + {}^{[6]}r(O^{2-}) = 1.17$ Å + 1.4 Å = 2.57 Å], but larger than the sum of Mn^{2+} and O^{2-} ion radii [$r(Mn^{2+}) + {}^{[6]}r(O^{2-}) = 0.67$ Å + 1.4 Å = 2.07 Å][6]. Therefore, Mn^{2+} ions preferentially occupy the M3 sites, driving Eu^{2+} ions to the M2 and M1 sites. As mentioned in the previous section, the Eu–O bond length significantly affects the crystal field strength (D_q), that is, D_q is proportional to $1/d^5$, and the looser site accommodating Eu^{2+} ions should correspond to a higher-energy (shorter wavelength) emission peak, while a lower-energy (longer wavelength) emission appears.[21] Therefore, at $y = 0.63$, the Eu^{2+} ions mainly stay in the M1 sites, as confirmed by the similar d(M1–O) [2.59 Å, 440 nm] in the Mn series and d(M2–O) [2.60 Å, $x = 0.15$, 442 nm] in the Ba series.

To ensure high efficiency for the phosphor-converted WLED devices, a comprehensive understanding of the thermal quenching of phosphors is necessary.[22–25] The relative emission intensity (I_T/I_0) for the Ba and Mn series from room temperature to 573 K are shown in Fig. 5a and b. The emission intensity decreases with the environmental temperature increase for all the samples because of the thermal quenching effect. However, the overall trend of thermal stability improvement by doping is evident in the Ba series ($x = 0$–1.59) and the Mn series ($y = 0$–0.63), with respect to the parent $Sr_{2.97}Eu_{0.03}Y_2(Si_3O_9)_2$ sample. In particular, the Ba series shows a clear thermal stability increase at the phase transition. The results can be governed by the increasing quenching activation barriers in both series (insert in Fig. 5b). Generally, excellent thermal stability could be expected in certain phosphors with high covalency, high rigidity and a small Stokes shift. The blue shifts in the Ba and Mn series cause the Stokes shift decrease, indicating a thermal energy increase (E_a). The E_a values of the Ba and Mn series were calculated by relation $I_T/I_0 = [1 + D\exp(-E_a/kT)]^{-1}$, where I_T (intensity at T), I_0 (intensity at $T = 0$), D, and activation energy E_a are refined variables.[10] Clearly, the E_a values of the Ba and Mn series gradually increase with x and y (insert in Fig. 5b), suggesting that the probability of nonradiative transition is weakened. Therefore, the thermal stability of the phosphors gradually increased on doping. A clear thermal quenching decrease appeared at the phase transition point, as shown by the dashed circle in Fig. 5a. This finding is also consistent with the E_a turning point during the phase transition (the insert in Fig. 5b). Thus, a jump change of thermal stability is possible in phosphor materials at phase transition. It is noted that the Mn series have a lower enhancement for the thermal stability than the Ba series, which can be attributed to the different thermal decay behavior between Eu^{2+} and Mn^{2+}.

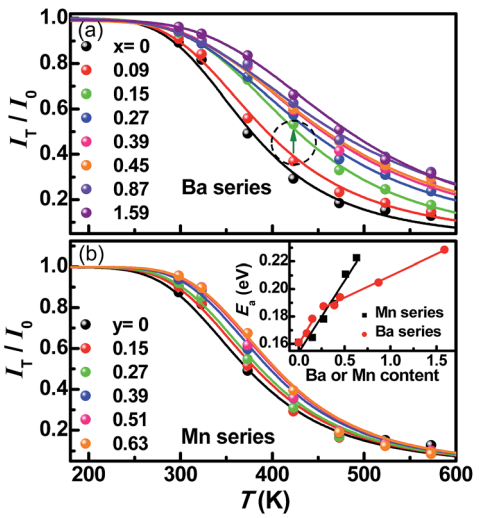

Fig. 5 Thermal quenching behaviour of photoluminescence for (a) $Sr_{2.97-x}Ba_xEu_{0.03}Y_2(Si_3O_9)_2$ ($x = 0$–1.59) and (b) $Sr_{2.97-y}Mn_yEu_{0.03}Y_2(Si_3O_9)_2$ ($y = 0$–0.63) samples. Insert in (b) is the plot of activation energies dependent on x for Ba series and y for Mn series.

To sum it up, the lattice-site control effect for Eu^{2+} ions discovered in $M_5(Si_3O_9)_2$ (M = Sr, Ba, Y, Mn) crystals can efficiently tune the photoluminescence and thermal quenching properties *via* the cation-substitution approach. This effect provides a new insight into the structural variations of the single-cation sites that are induced by phase transition and site-preferential occupancy, which are driven *via* size-mismatched cation substitution and can tune the luminescent properties of phosphor materials. This work reveals the mechanisms of optical adjustment by the coordination environment changing at specific sites. In particular, the abrupt structural change owing to phase transition offers unexpected and large-scale changes in optical properties. This effect can be extended to tune other properties, including the electric and magnetic properties that are sensitive to the structural variation at local sites.[26–28]

Acknowledgements

This project is financially supported by the National Natural Science Foundation of China (Grants No. NSFC 21301162, 21571162, 60977013, 91433110, U1301242, 21221061), the National College Students' Innovative Training Program (Nos. 201510491109, 201610491067, 201610491070), and the Ministry of Science and Technology of Taiwan (No. MOST 104-2917-I-564-060). Zewei Quan acknowledges the funding support (FRG-SUSTC1501A-17) from South University of Science and Technology of China.

Notes and references

1 N. C. George, K. A. Denault and R. Seshadri, *Annu. Rev. Mater. Res.*, 2013, **43**, 481–501.
2 R. J. Xie and N. Hirosaki, *Sci. Technol. Adv. Mater.*, 2007, **8**, 588–600.
3 P. Pust, V. Weiler, C. Hecht, A. Tücks, A. S. Wochnik, A.-K. Henß, D. Wiechert, C. Scheu, P. J. Schmidt and W. Schnick, *Nat. Mater.*, 2014, **13**, 891–896.
4 Z. G. Xia, C. G. Ma, M. S. Molokeev, Q. L. Liu, K. Rickert and K. R. Poeppelmeier, *J. Am. Chem. Soc.*, 2015, **137**, 12494–12497.
5 G. G. Li, Y. Tian, Y. Zhao and J. Lin, *Chem. Soc. Rev.*, 2015, **44**, 8688–8713.
6 Y. Sato, H. Kato, M. Kobayashi, T. Masaki, D. H. Yoon and M. Kakihana, *Angew. Chem., Int. Ed.*, 2014, **53**, 7756–7759.
7 K. A. Denault, J. Brgoch, M. W. Gaultois, A. Mikhailovsky, R. Petry, H. Winkler, S. P. DenBaars and R. Seshadri, *Chem. Mater.*, 2014, **26**, 2275–2282.
8 Z. Y. Zhao, Z. G. Yang, Y. R. Shi, C. Wang, B. T. Liu, G. Zhu and Y. H. Wang, *J. Mater. Chem. C*, 2013, **1**, 1407–1412.
9 W. T. Chen, H. S. Sheu, R. S. Liu and J. P. Attfield, *Inorg. Chem.*, 2012, **51**, 8802–8809.
10 S. S. Wang, W. T. Chen, Y. Li, J. Wang, H. S. Sheu and R. S. Liu, *J. Am. Chem. Soc.*, 2012, **134**, 8022–8025.
11 F. W. Kang, H. S. Zhang, L. Wondraczek, X. B. Yang, Y. Zhang, D. Y. Lei and M. Y. Peng, *Chem. Mater.*, 2016, **28**, 2692–2703.
12 Z. G. Xia, G. K. Liu, J. G. Wen, Z. G. Mei, M. Balasubramanian, M. S. Molokeev, L. C. Peng, L. Gu, D. J. Miller, Q. L. Liu and K. R. Poeppelmeier, *J. Am. Chem. Soc.*, 2016, **138**, 1158–1161.
13 A. P. Tyutyunnik, I. I. Leonidov, L. L. Surat, I. F. Berger and V. G. Zubkov, *J. Solid State Chem.*, 2013, **197**, 447–455.
14 H. Yamane, T. Nagasawa, M. Shimada and T. Endo, *Acta Crystallogr., Sect. C: Cryst. Struct. Commun.*, 1997, **53**, 1533–1536.
15 P. P. Dai, C. Li, X. T. Zhang, J. Xu, X. Chen, X. L. Wang, Y. Jia, X. J. Wang and Y. C. Liu, *Light: Sci. Appl.*, 2016, **5**, e16024.
16 M. Seibald, T. Rosenthal, O. Oeckler and W. Schnick, *Crit. Rev. Solid State Mater. Sci.*, 2014, **39**, 215–229.
17 W. B. Park, S. P. Singh and K. S. Sohn, *J. Am. Chem. Soc.*, 2014, **136**, 2363–2373.
18 G. K. Liu, *Chem. Soc. Rev.*, 2015, **44**, 1635–1652.
19 W. B. Im, Y. Kim, H. S. Yoo and D. Y. Jeon, *Inorg. Chem.*, 2009, **48**, 557.
20 H. Terraschke and C. Wickleder, *Chem. Rev.*, 2015, **115**, 11352.
21 P. Dorenbos, *ECS Solid State Lett.*, 2013, **2**, R3001–R3011.
22 Z. J. Zhang, O. M. ten Kate, A. Delsing, E. van der Kolk, P. H. L. Notten, P. Dorenbos, J. T. Zhao and H. T. Hintzen, *J. Mater. Chem.*, 2012, **22**, 9813–9820.
23 M. Y. Peng, X. W. Yin, P. A. Tanner, M. G. Brik and P. F. Li, *Chem. Mater.*, 2015, **27**, 2938–2945.
24 C. R. Ronda, *Luminescence: From Theory to Applications*, Wiley-VCH Verlag GmbH & Co. KGaA, Weinheim, 2008.
25 Y. Q. Li, N. Hirosaki, R. J. Xie, T. Takeda and M. Mitomo, *Chem. Mater.*, 2008, **20**, 6704–6714.
26 S. Zhang, T. Saito, M. Mizumaki, W. T. Chen, T. Tohyama and Y. Shimakawa, *J. Am. Chem. Soc.*, 2013, **135**, 6056–6060.
27 W. Zheng, P. Huang, D. T. Tu, E. Ma, H. M. Zhu and X. Y. Chen, *Chem. Soc. Rev.*, 2015, **44**, 1379–1415.
28 F. W. Kang, X. B. Yang, M. Y. Peng, L. Wondraczek, Z. J. Ma, Q. Y. Zhang and J. R. Qiu, *J. Phys. Chem. C*, 2014, **118**, 7515–7522.